

Single-molecule probing of the conformational homogeneity of the ABC transporter BtuCD

Min Yang^{1,5}, Nurit Livnat Levanon^{2,5}, Burçin Acar³, Burcu Aykac Fas³, Gal Masrati⁴, Jessica Rose², Nir Ben-Tal^{4*}, Turkan Haliloglu^{3*}, Yongfang Zhao¹ and Oded Lewinson^{2*}

ATP-binding cassette (ABC) transporters use the energy of ATP hydrolysis to move molecules through cellular membranes. They are directly linked to human diseases, cancer multidrug resistance, and bacterial virulence. Very little is known of the conformational dynamics of ABC transporters, especially at the single-molecule level. Here, we combine single-molecule spectroscopy and a novel molecular simulation approach to investigate the conformational dynamics of the ABC transporter BtuCD. We observe a single dominant population of molecules in each step of the transport cycle and tight coupling between conformational transitions and ligand binding. We uncover transient conformational changes that allow substrate to enter the transporter. This is followed by a ‘squeezing’ motion propagating from the extracellular to the intracellular side of the translocation cavity. This coordinated sequence of events provides a mechanism for the unidirectional transport of vitamin B₁₂ by BtuCD.

ABC transporters are ubiquitous proteins that harness the energy of ATP hydrolysis to move a diversity of molecules through cell membranes^{1–3}. They are involved in numerous physiological processes^{4,4–9} and are directly linked to human diseases, to tumor resistance to chemotherapy, and to bacterial virulence^{7,10–12}. An ABC transporter is minimally composed of two intracellular nucleotide-binding domains (NBDs) that bind and hydrolyze ATP and two transmembrane domains (TMDs) that form the permeation pathway (Fig. 1a)¹³. ABC transporters that function as importers require a substrate-binding protein (SBP), which recognizes the substrate with high affinity and delivers it to the TMDs^{14,15}. The mechanism of action of ABC transporters is described by the ‘alternating access’ model^{6,13,16}, in which ATP binding and hydrolysis drive the opening and closing of the NBDs¹⁷, which in turn leads to transition of the TMDs between the inward and outward facing conformations.

It is broadly recognized that the dynamics and rates of conformational changes are fundamental properties of enzyme catalysis and protein function¹⁸. However, the experimental exploration of conformational dynamics is difficult and often requires single-molecule approaches. The ability to watch single molecules provides unique information on conformational distributions, resolves heterogeneous samples, and records asynchronous conformational changes that would be obscured in bulk measurements^{19–23}. There are very few reported single-molecule studies of ABC transporters^{23–26}, and therefore our understanding of the conformational dynamics of ABC transporters remains limited.

Here, we combined single-molecule Förster resonance energy transfer (smFRET) and a newly developed molecular simulation approach to investigate the conformational dynamics of BtuCD-F, the *Escherichia coli* vitamin B₁₂ ABC importer²⁶. BtuCD-F is one of the best-characterized ABC transporters, serving as a model for ABC importers of heme and iron siderophores^{27–30}, as well as for ABC importers of transition metals, which are essential for bacterial virulence^{10,31}.

We found that the conformational dynamics of BtuCD-F are very different from those reported for secondary transporters, revealing a transporter of conformational homogeneity, with tight coupling between conformational changes and ligand binding.

Results

Single-molecule measurements. To measure smFRET, we introduced single cysteines to Cys-less BtuCD at positions that have low sequence conservation and are distant to known functional sites. We chose positions that are compatible with the Förster distance of the Cy3–Cy5 donor–acceptor pair and that are expected to undergo movements of ~1 nm upon binding of ATP and/or BtuF^{29,32–34}. Because BtuCD is a homodimer, a single genetic mutation results in twin substitutions at the protein level. We selected mutants that were efficiently and specifically labeled and had wild-type levels of pre- and post-labeling activity (Supplementary Fig. 1; Supplementary Table 1). The fluorescently labeled mutants displayed low anisotropy (Supplementary Table 2), indicating that the rotation of the dyes is not substantially limited by the protein and that FRET modifications can be used to monitor conformational changes. For analysis, we chose mutants located at the NBDs (S67C) and at the cytoplasmic (R138C) and periplasmic (Q109C) sides of the TMDs (Fig. 1a). Initially, all measurements were conducted in detergent solution using the same detergent that was used for determination of all BtuCD-F crystal structures^{29,32–34}. Next, to mimic the membrane environment, we reconstituted BtuCD into nanodiscs^{35,36}. In both detergent and nanodiscs, labeled transporters were specifically immobilized to a microfluidic surface (Fig. 1b; Supplementary Fig. 2), and single molecules were imaged using total internal reflection fluorescent (TIRF) microscopy.

Conformational dynamics of the nucleotide binding domains. Averaged histograms were generated from hundreds of smFRET time traces of single BtuCD S67C (NBDs located) molecules. Such

¹National Laboratory of Macromolecules, CAS Center for Excellence in Biomacromolecules, Institute of Biophysics, Chinese Academy of Sciences, Beijing, China. ²Department of Biochemistry and the Rappaport Institute for Medical Sciences, Faculty of Medicine, The Technion-Israel Institute of Technology, Haifa, Israel. ³Department of Chemical Engineering and Polymer Research Center, Bogazici University, Istanbul, Turkey. ⁴Department of Biochemistry and Molecular Biology, George S. Wise Faculty of Life Sciences, Tel Aviv University, Tel Aviv, Israel. ⁵These authors contributed equally: Min Yang, Nurit Livnat Levanon. *e-mail: bental@tauex.tau.ac.il; halilogt@boun.edu.tr; lewinson@technion.ac.il

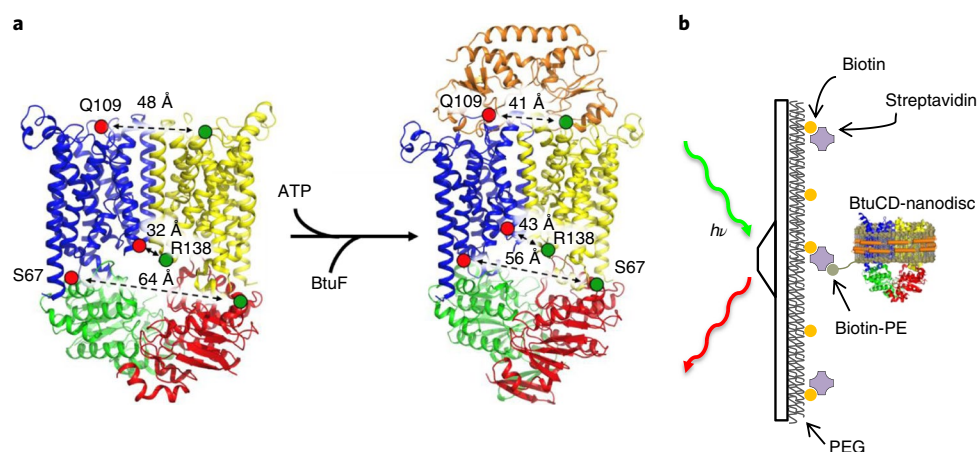


Fig. 1 | smFRET experimental design. **a**, Ribbon representation of apo BtuCD (PDB ID 1L7V, left) and AMP-PNP-bound-BtuCD-F (PDB ID 4F13, right). BtuCD is composed of a homodimeric transmembrane domain (yellow and blue) and a homodimeric nucleotide binding domain (green and red); BtuF is in orange. The labeled positions are shown as red and green spheres. Also shown are the crystal structure distances between the twin positions. **b**, Set up of smFRET measurements: Cy3-Cy5-labeled BtuCD is reconstituted into nanodiscs and is then immobilized to a streptavidin-treated, PEG-coated surface via biotin-PE.

histograms represent the conformational distribution of the population of molecules for a given experimental condition. Initially, to simplify the interpretation, we conducted the measurements under equilibrium conditions and trapped the transporter in the various steps of the catalytic cycle. To push the population of BtuCD molecules toward complete conformational changes, we added the nucleotides at saturating concentrations^{30,37,38}. In the absence of ligands (apo state), we observed a single population of transporter molecules with a low average smFRET of ~ 0.25 (Fig. 2a; Supplementary Table 3). To induce the prehydrolysis ATP-bound state, we added ATP (in the absence of Mg^{2+}) or the nonhydrolyzable ATP analog AMP-PNP- Mg^{2+} . In both cases, a uniform population of molecules that had shifted to a higher FRET state of ~ 0.35 was observed (Fig. 2b,c; Supplementary Table 2), indicating a reduced distance between the twin S67 residue pair and closure of the NBDs. An identical smFRET distribution was observed in the posthydrolysis high-energy intermediate state (in the presence of ATP-vanadate- Mg^{2+} ; Fig. 2d). This indicates that in both the pre- and posthydrolysis states the NBDs are closed. Next, we tested the effects of docking of BtuF on the conformational state of the NBDs. This was performed in two different ways: in one procedure, we isolated the stable BtuCD-F complex^{30,37} and then immobilized the BtuCD-F complex to the microfluidic surface. In another protocol, we immobilized apo BtuCD and then added 1–10 μM of BtuF. Using either protocol we did not observe any effect of BtuF on the smFRET state of the NBDs, regardless of whether ATP was bound or not (Fig. 2b,e,f; Supplementary Table 3). Taken together, these results demonstrate that the closure of the NBDs is independent of BtuF docking yet fully dependent on binding of ATP. Notably, in each of the tested conditions, we observed only one dominant population of BtuCD molecules, which readily fit a single Gaussian distribution (Fig. 2a–f, solid black traces). This conformational homogeneity differs from the conformational heterogeneity observed for the ABC exporters BmrCD, Pgp, and TM287/288 (refs 39–41). Such conformational homogeneity implies a considerable energy difference between the open and closed NBD conformations. If the energetic difference had been small, several FRET states would have been present in each condition. The time traces of individual BtuCD molecules revealed that the NBDs do not spontaneously fluctuate between their open and closed states, and this ‘conformational stability’ was observed in all of the tested conditions (Fig. 2g). In thousands of traces, we did not detect

clear dwell times in more than one conformation. This tight coupling between closure of the NBDs (and hence formation of the ATP binding site) and the presence of ATP strongly suggests an induced-fit mechanism for this conformational change. However, we cannot exclude the possibility that spontaneous conformational fluctuations occur on a time scale that is faster than our maximal temporal imaging resolution (50 ms). To induce spontaneous fluctuations, we added subsaturating concentrations of nucleotides. In the presence of 1 nM ATP (in the absence of Mg^{2+}), we did not observe clear conformational fluctuations: the individual traces were practically identical to those observed in the apo state (Fig. 3a, top panel), and the FRET state of the population was similar to that observed in the absence of bound ATP (compare Fig. 3a to Fig. 2a). However, at 50 nM ATP we observed short-lived transitions to the NBDs closed state (Fig. 3b, top panel), yet these short fluctuations did not significantly affect the population ensemble-averaged FRET state (Fig. 3b, bottom panel). At 1 μM ATP, we observed extended dwell times at the closed NBD state (Fig. 3c, top panel) and increased population heterogeneity, and found that the FRET state of the population was similar to that of ATP-bound BtuCD (compare Fig. 3c, bottom panel, to Fig. 2b, left panel). That the majority of the molecules had closed their NBDs in the presence of 1 μM ATP suggests that the ATP-binding affinity is significantly higher than the apparent affinity of 20 μM that was inferred from the Michaelis–Menten constant (K_m) derived from ATP hydrolysis assays³⁸. To corroborate that the occupancy of the high FRET state is in line with the K_D for ATP, we measured it directly by using isothermal titration calorimetry and determined a K_D of $0.3 \pm 0.17 \mu M$ (Fig. 3d), which agrees with the near complete reversion to the high FRET state observed at 1 μM ATP.

To gain insight into the rate of closure of the NBDs in the presence of physiological ATP concentrations (millimolar range⁴²), we conducted nonequilibrium experiments wherein during the imaging we added 1 mM ATP (in the absence of Mg^{2+}) to apo BtuCD. A clear reversion to the high FRET state (corresponding to the closure of the NBDs) was observed upon addition of the nucleotide (Fig. 3e–g). In $\sim 25\%$ of the molecules, 1 mM ATP concentration induced a conformational change that could not be temporally resolved using our maximal temporal resolution of 50 ms (Supplementary Fig. 3a,b). However, the conformational transition of $>50\%$ of the molecules was resolved by several data points (Supplementary Fig. 3c–f), and from these transitions we estimate that the slower conformational

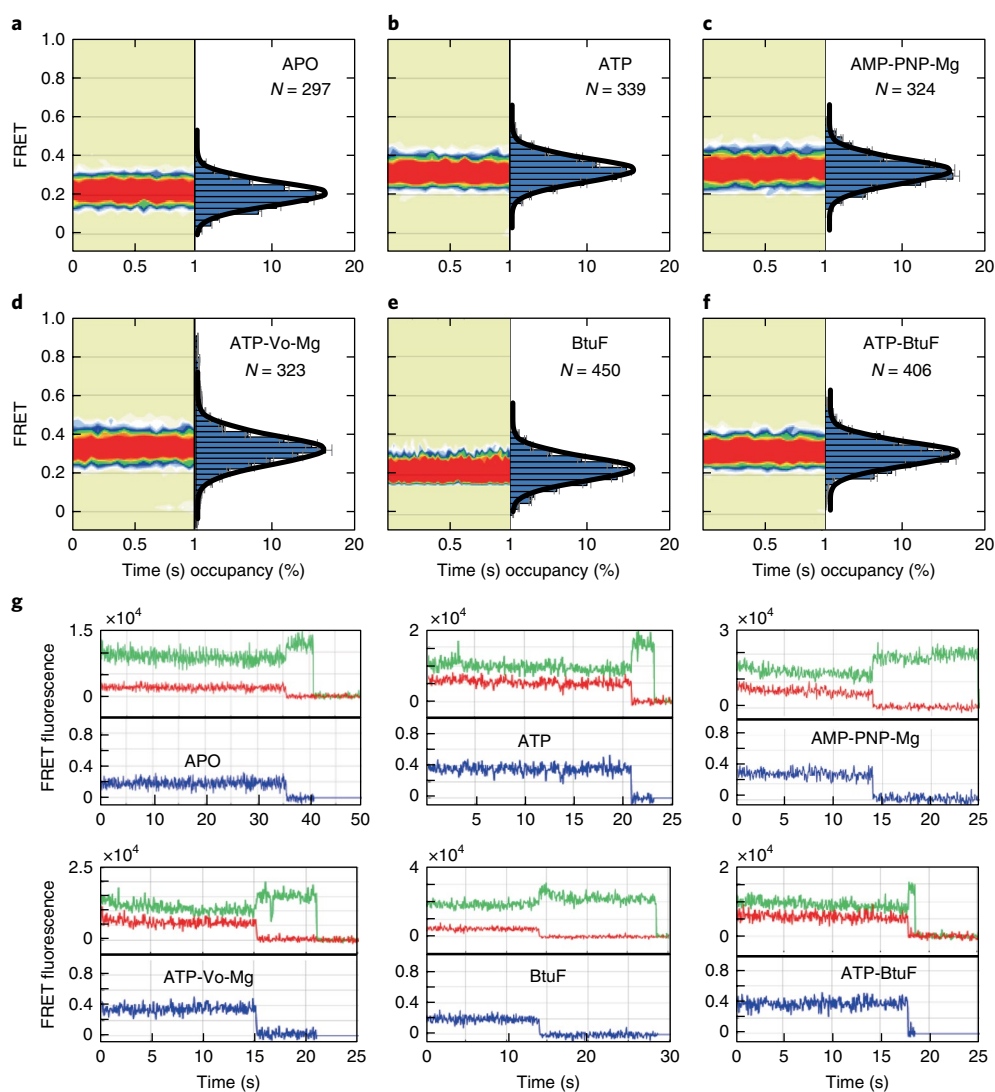


Fig. 2 | Conformational distributions and conformational stability of the NBDs. **a–f**, left panels: time-dependent population contour plots, obtained from the analysis of N single-molecules traces (measured in detergent). The plots are colored from lowest (tan) to highest (red) population. **a–f**, right panels: time-averaged cumulative population histograms (blue bars) and fits to single Gaussian distributions (solid black traces). Shown are representative results of at least three distinct experiments, performed in the absence of ligands (**a**), or in the presence of 1 mM ATP (no Mg^{2+}) (**b**), 1 mM AMP-PNP- Mg^{2+} (**c**), 1 mM ATP- V_o - Mg^{2+} (**d**), 1 μ M BtuF (**e**), 1 mM ATP (no Mg^{2+}) + 1 μ M BtuF (**f**). Error bars are s.d. obtained by a bootstrap estimation approach with 100 samples. **g**, Representative single-molecule time traces of the fluorescence (Cy3 green, Cy5 red, and FRET blue) obtained at the indicated conditions using the same concentrations of ligands as those in **a–f**.

changes occur on a time scale of 200–400 ms. Next, we conducted smFRET experiments in a membrane-mimetic environment using BtuCD reconstituted into nanodiscs^{34,36}. The results obtained in the nanodiscs were largely similar to those obtained in detergent solution. Also in the nanodiscs, closure of the NBDs was fully dependent on ATP binding, and docking of BtuF to apo BtuCD had little to no effect (Fig. 3h; Supplementary Fig. 4). In the nanodiscs, a tail of higher FRET values (FRET = 0.75–0.8) was present in all conditions (Supplementary Fig. 4). It is highly unlikely that such high values originate from FRET between the S67C twin residues (due to the distance between them) and likely stem from non-specific events⁴³. A notable difference between the detergent solution and the nanodiscs was that only in the latter did binding of BtuF to ATP-bound BtuCD result in a slight, yet statistically significant decrease in smFRET ($P = 2.96 \times 10^{-5}$, Kolmogorov–Smirnov test; Fig. 3h, compare magenta and blue curves; Supplementary Fig. 4, compare panels b and e). This implies that in the membrane-mimetic environment, docking of BtuF leads to a partial opening

of the NBDs, lowering the affinity of BtuCD to ATP, perhaps facilitating nucleotide release. This suggestion is thermodynamically compatible with the experimentally observed reciprocal effect in which the release of BtuF and other SBPs of type-II ABC importers is driven by ATP binding and hydrolysis^{26,28,37,44,45}. Using the nanodiscs, we also tested for the effects of the transport substrate (vitamin B_{12}), and found that it had little to no effect on the smFRET measured at the NBDs (Fig. 3h, red vs. green and blue vs. olive-green curves). These results are in line with previous reports of the vitamin having minimal effect on the conformations and ATPase activity of BtuCD^{26,30,37}. As observed in detergent, in the nanodiscs we did not observe spontaneous fluctuations between the open and close states of the NBDs in any of the tested conditions (Supplementary Fig. 5).

Taken together, these results demonstrate that in both detergent and nanodiscs the NBDs close only upon ATP binding and open only upon its release, and that they do not spontaneously fluctuate between the open and closed states.

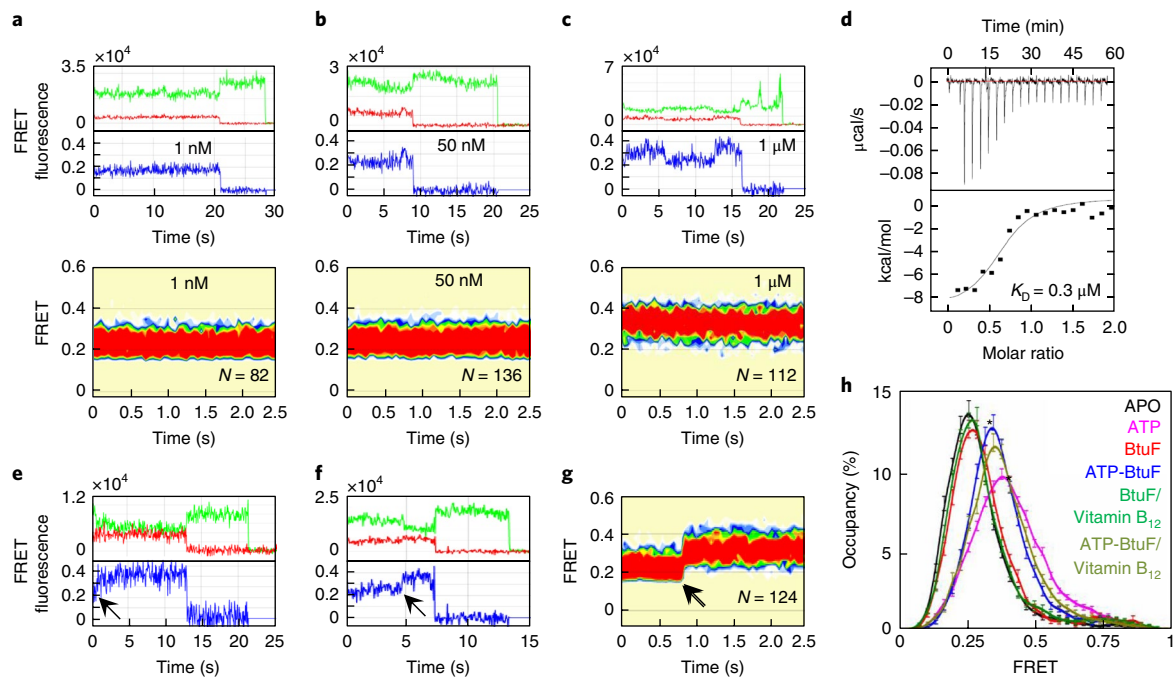


Fig. 3 | Conformational dynamics of the NBDs. **a–c**, Top panels: single-molecule time traces of the fluorescence (Cy3 green, Cy5 red, and FRET blue) of BtuCD S67C. Bottom panels: time-dependent population contour plots colored from lowest (tan) to highest (red) population, obtained from the analysis of N single BtuCD S67C molecules traces measured in detergent. Experiments were conducted in the presence of 1 nM (**a**), 50 nM (**b**), or 1 μ M ATP (**c**) (all in the absence of Mg^{2+}). **d**, Affinity of ATP binding by BtuCD as measured by isothermal titration calorimetry. Shown is the dissociation constant determined in three distinct experiments (s.d. = 0.17 μ M). **e, f**, Single-molecule traces of the fluorescence of BtuCD S67C, color coded as in **a–c**. At time zero, no ligands were present. At 1 s (**e**) or 4 s (**f**), as indicated by the arrows, 1 mM ATP (no Mg^{2+}) was added. **g**, Time-dependent population contour plot of N single BtuCD S67C molecules to which 1 mM ATP (in the absence of Mg^{2+}) was added at the time indicated by the arrow. The population contour plots are colored from tan (lowest) to red (highest) population. **h**, Overlay of the distributions of BtuCD S67C reconstituted in nanodiscs, at the indicated conditions. Nucleotides were added at 1 mM, BtuF at 1 μ M, and vitamin B_{12} at 10 μ M. Shown are representative results of experiments repeated at least three times. Error bars are s.d. obtained by a bootstrap estimation approach with 100 samples. In **h**, $*P = 2.96 \times 10^{-5}$ for the difference between the ATP-bound (magenta) and ATP/BtuF-bound (blue) distributions, using the Kolmogorov–Smirnov test.

Conformational dynamics of the transmembrane domains. In the transition from the outward- to the inward-facing conformations of BtuCD, the periplasmic ends of TM helices 3 and 4 swing inward, whereas their cytosolic ends swing outward^{29,32–34} (Supplementary Fig. 6). This motion is part of a collective rearrangement of the TMDs that seals the translocation cavity to the periplasm while partially opening it to the cytoplasm. To monitor this motion, we labeled residues R138C and Q109C located at the cytoplasmic and periplasmic ends of TM helix 4, respectively (Fig. 1a). These two residues are expected to move in opposite directions in the outward-to-inward transition (Supplementary Fig. 6) and provide complementary information on the orientation of the TMDs.

In both detergent and nanodiscs, BtuF docking led to a conformational change that increased the smFRET between the Q109C labels, signifying that the periplasmic side of the TMDs had closed (Fig. 4a). In contrast, the cytosolic side of the TMDs was largely unaffected by docking of BtuF (Fig. 4b). ATP binding led to the opening of the cytoplasmic side of the TMDs (Fig. 4b) yet had little effect on their periplasmic side (Fig. 4a). Therefore, ATP and BtuF demonstrate complementary roles in controlling the conformational status of the TMDs, with BtuF controlling the periplasmic side of the TMDs and ATP regulating their cytoplasmic side. These results are in excellent agreement with previous ensemble EPR and DEER studies of BtuCD-F^{45,46}. As observed at the NBDs, the presence of the substrate (vitamin B_{12}) had no effect on the conformation at either side of the TMDs (Fig. 4a,b). Notably, for the Q109C label, the amplitude of the FRET changes was larger in the membrane environment than in detergent (Fig. 4a; Supplementary Table 3). In apo BtuCD,

the FRET at the periplasmic side (Q109C) was 0.45 in nanodiscs and 0.5 in detergent ($P = 0.042$; Fig. 4a; Supplementary Table 3). This wider periplasmic opening at the apo state was correlated with a much tighter periplasmic seal upon docking of BtuF \pm ATP (FRET of ~ 0.72 in nanodiscs vs. ~ 0.58 in detergent, $P = 3.45 \times 10^{-28}$; Fig. 4a; Supplementary Table 3). The observed differences may arise from differences in dye-tumbling behavior in the various environments. However, anisotropy measured in detergent and in nanodiscs revealed no systematic trend that could account for these differences (Supplementary Table 2). In addition, the anisotropy values ($r = 0.186–0.233$) are consistent with considerable randomization of dye orientation on the 50-ms time scale of imaging.

These results suggest that in the membrane, relative to what is observed in the crystal structures, ligand-free outward-facing BtuCD is more open to the periplasm and closes more tightly upon binding of BtuF and ATP (Fig. 4c). As observed for the NBDs, we did not see spontaneous smFRET fluctuations of the TMDs, implying tight coupling between the conformational changes and the binding of ligands (Fig. 5a–d). To capture dynamic events of conformational transitions in the TMDs, we conducted experiments in which vitamin B_{12} was added in 20:1 molar excess over BtuF, which greatly accelerates the k_{off} of BtuF from BtuCD³⁷. Under these conditions, we were able to observe spontaneous transitions between the closed and open states of the TMDs (Fig. 5e). We also performed nonequilibrium experiments in which BtuF was added during the imaging to apo BtuCD, and observed a clear switch of single molecules to the higher FRET state, indicating closure of the periplasmic side of the TMDs (Fig. 5f). The closure of the TMDs

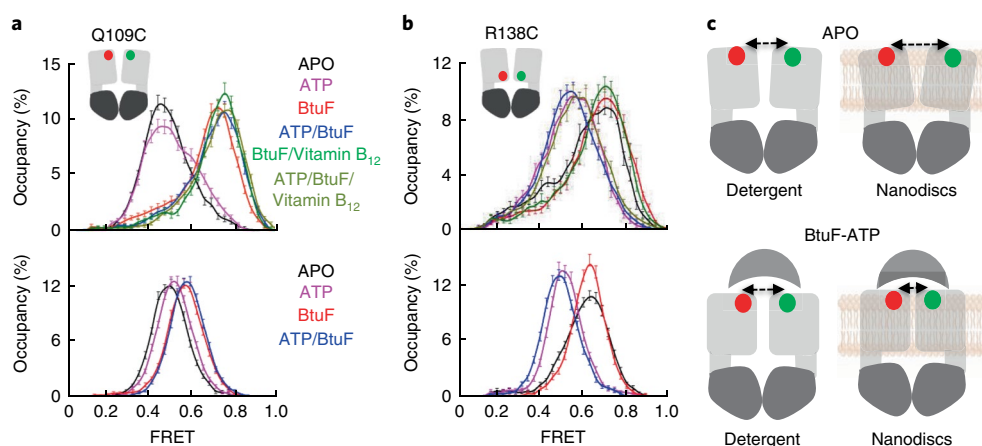


Fig. 4 | Conformational distributions of the TMDs and differences between the membrane and detergent environments. a, b, smFRET distributions of the periplasmic (**a**) and cytosolic (**b**) sides of the TMDs measured in nanodiscs (top panels) or detergent solution (bottom panels). Measurements were conducted in the absence of ligands (apo state) or in the presence of the indicated ligands (color coded). Nucleotides were added at 1 mM, BtuF at 1 μ M, and vitamin B₁₂ at 10 μ M. Shown are representative results of experiments repeated at least three times. Error bars are s.d. obtained by a bootstrap estimation approach with 100 samples. **c**, Main differences between the conformations in detergent solution and those in the membrane. In the apo state, the periplasmic side of the TMDs is more open to the periplasm in nanodiscs than in detergent (top panels). Upon binding of ATP and docking of BtuF, the closure of the TMDs is more complete in nanodiscs than in detergent (bottom panels). Red and green spheres indicate the positions of the twin Q109 residues.

was also apparent at the level of the population (Fig. 5g), demonstrating that the onset and rates of the conformational changes are fairly synchronized across the population of the single molecules. Taken together, these results show that the conformational changes at the TMDs are tightly linked to ligand binding and do not occur spontaneously.

Transient movements allow delivery of vitamin B₁₂. The crystal structure of apo BtuCD is interpreted as representing an outward-facing conformation²⁹. However, in this conformation, the periplasmic access to the translocation cavity is blocked by a gate formed by leucine 172 from each BtuC monomer (Supplementary Fig. 7a); namely, it represents an occluded, outward-facing conformation. In this conformation, there is a steric clash between the L172 gate residues and the BtuF-bound vitamin B₁₂ (Supplementary Fig. 7b), making docking of BtuF practically impossible. In the ATP-bound³⁴ and ATP/BtuF-bound³⁵ states this steric clash persists, and the translocation cavity remains blocked by the L172 gate residues. This highlights an unresolved mechanistic enigma: how is vitamin B₁₂ delivered to the translocation cavity? Enhancing this conundrum, the results reported herein demonstrate that all of the conformational changes from the apo (outward-occluded) state lead to conformations that are yet more closed. It is possible that during the ATPase cycle, or during the initial association of BtuF with BtuCD, the L172 gate residues transiently move apart to allow passage of vitamin B₁₂ and then re-seal the translocation cavity (as observed in all the crystal structures). Such conformational changes may remain undetected by smFRET if the changes in distance are small or if the rate of opening and closing exceeds the temporal resolution of imaging. To explore these possibilities, we sought to apply a computational approach. However, the ~200- μ s duration of molecular dynamics (MD) simulations is too short for studying the conformational changes of BtuCD that occur on a timescale of hundreds of milliseconds (Figs. 3e–g and 5f,g; Supplementary Fig. 3). We therefore developed a novel methodology that integrates low-resolution α -carbon based anisotropic network model (ANM)¹⁷ with stochastic all-atom implicit solvent Langevin dynamics (LD) simulations⁴⁸. In this hybrid approach (ANM–LD), an explicit definition of time is waived for the sake of enhanced sampling of the conformational space. Therefore, one cannot deduce

the rates of conformational changes, yet the trajectory of conformational transition can be calculated (see Supplementary Fig. 8 and Methods for more details). We constructed a complete atomistic view of the conformational changes that occur upon binding of BtuF and/or ATP (Supplementary Videos 1–3). From these simulations, we extracted the distance between the L172 gate residues during the transport cycle. Individually, BtuF and ATP had opposite effects on the opening of the periplasmic gate: docking of BtuF led to its tighter closure, whereas ATP binding led to its opening (Fig. 6a). However, the combined and complementary effects of ATP and BtuF are revealed when both bind simultaneously—i.e., in the transition between the apo and ATP + BtuF-bound states. In the first ~20 cycles of this transition, the distance between the L172 twin residues remains fairly constant. Then, the two residues steeply move apart and remain open for ~30 cycles before rapidly collapsing back to their initial closed conformation. This transient opening is unique to the periplasmic gate L172 pair, as we could not identify any other TMD residue that displays this pattern. This suggests that during the transition from the apo to the ATP/BtuF-bound state, ATP binding drives the transient opening of the periplasmic gate (to allow delivery of vitamin B₁₂) and BtuF drives its re-closure (to prevent escape of vitamin B₁₂). Next, we tried to identify the specific movements in BtuCD that enable substrate delivery. We examined the ensemble of isolated movements that together comprise the complete conformational transition and pinpointed two specific movements that are responsible for the transient opening of the periplasmic gate and delivery of the vitamin from BtuF to the translocation cavity. In the first mode of movement, the L172 pair moves sideways in an antiparallel manner, leading to the opening of the gate (Supplementary Video 4). Another important aspect of this movement is the downward and outward tilt of the periplasmic loop that connects TM helices 2 and 3 (Supplementary Video 4). The movement of this loop clears the way for the oncoming SBP and prepares the periplasmic surface for the docking of its helices 3 and 8 (ref. 32). In the second mode of movement, the L172 pair moves up in parallel (Supplementary Video 5), increasing the steric clash with BtuF-bound vitamin B₁₂ and abolishing its binding site. The TM2–TM3 loops close back to lock on the now-docked SBP. Combined, these two modes of movements act as a claw crane: first, the claws open, and then swoop upward to clutch their prize.

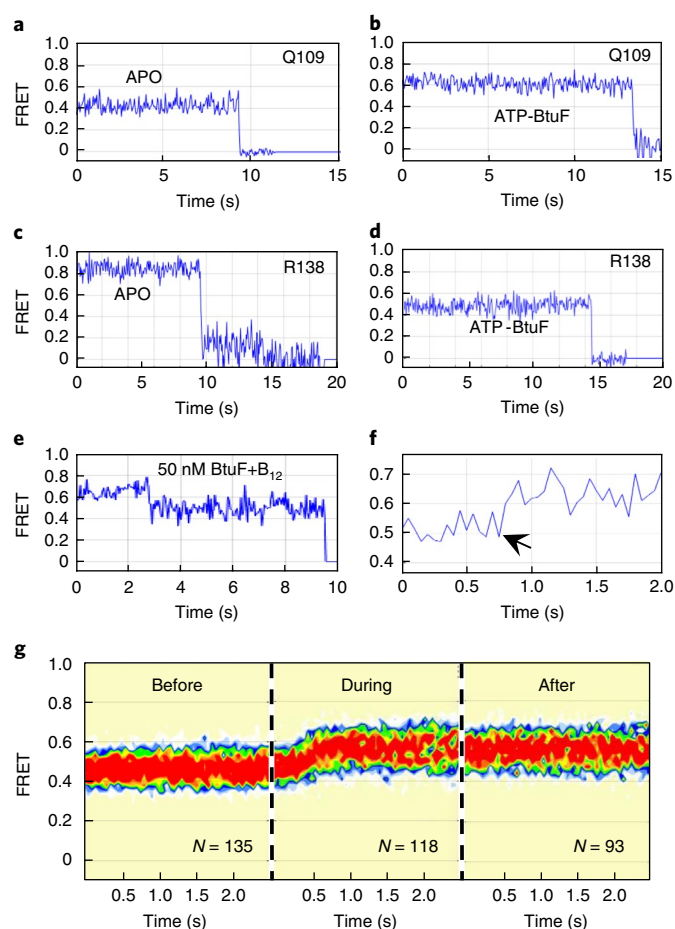


Fig. 5 | Conformational dynamics of the TMDs. (a–d) Representative smFRET time traces of BtuCD Q109C (a,b) and BtuCD R138C (c,d) measured in detergent solution in the absence of ligands (a,c) or in the presence of 1 mM ATP (no Mg^{2+}) + 1 μ M BtuF (b,d). e, smFRET time trace of BtuCD Q109C in the presence of 50 nM BtuF and 1 μ M vitamin B_{12} . f, smFRET time trace of BtuCD Q109C to which 1 μ M BtuF was added at the time indicated by the arrow. g, Time-dependent population contour plot of N single BtuCD Q109C molecules imaged before (left), during (middle), and after (right) addition of 1 μ M BtuF. The population contour plots are colored from tan (lowest) to red (highest) population.

A ‘squeezing mechanism’ pushes the vitamin inwards. We next used the simulations to decipher the sequence of events that occur during the transition from the apo state to the BtuF/ATP-bound state. For this, we monitored the shifts in $C\alpha$ - $C\alpha$ distances ($C\alpha_r$) for the Q109, R138, and S67 pairs, as well as for the cytoplasmic gate residue S143. Not surprisingly, the movements of the residues located at the cytosolic side of the TMDs (R138 and S143) progress along parallel vectors and at the same rate (Fig. 6b, top). Attesting to the long-range allosteric connectivity in BtuCD, S67 (in the NBDs) and Q109 (periplasmic side of the TMDs) move along closely parallel vectors (Fig. 6b) despite the ~ 50 Å that separate them. Figure 6b reveals that there is a delay between the closing of the periplasmic side of the TMDs and the opening of their cytosolic side: in the first 20 cycles of the transition, the $C\alpha_r$ of Q109 (periplasmic side of the TMDs) decreased by ~ 6 Å, whereas the $C\alpha_r$ of the R138 pair (cytosolic side of the TMDs) did not change. At this point (\sim cycle 20), the L172 residues started to move apart (Fig. 6a), allowing access of vitamin B_{12} . By cycle 35 the translocation cavity was fully accessible, and vitamin B_{12} could be transferred from BtuF to the transporter. By this point, the Q109 residues had already closed

by ~ 8 Å, during which time the cytosolic residues R138 and S143 hardly moved (Fig. 6b).

The observation that the closing of the periplasmic side of the TMDs precedes the opening of their cytosolic side is also apparent in the two helices that line the translocation pathway. In the first 25 cycles of the simulation, the periplasmic sides of TM helices 5 and 5a move ~ 6 Å closer together, during which time their cytosolic side remains closed (Fig. 6c, compare cycles 0 and 25). In the next 20 cycles, the squeeze that originates from the periplasm continues: the periplasmic sides of TM helices 5 and 5a have by now constricted by more than 9 Å, whereas their cytosolic sides opened by less than 3 Å (Fig. 6c, cycle 45). The complete opening toward the cytosol occurs much later (Fig. 6c, cycle 150). Interestingly, during the whole simulation the distance between the residues that are situated at mid-height of TM helices 5 and 5a does not greatly change (Fig. 6c), leaving just enough space (14–15 Å) for the passage of vitamin B_{12} . To obtain a view of the time-dependent changes in the volume and shape of the translocation cavity, we combined the program HOLLOW⁴⁹ with our hybrid ANM-LD approach. We observed that Met180 of BtuC divides the translocation cavity to an upper and a lower compartment (Fig. 6d; Supplementary Video 6). As the conformational transition from the apo state to the BtuF/ATP-bound state progresses, the volume of the upper compartment shrinks, whereas that of the lower compartment remains largely unchanged (Fig. 6d; Supplementary Video 6). Shrinking of the upper compartment leads to an increased local concentration of vitamin B_{12} . Because at this point the translocation cavity is sealed to the periplasm by the L172 gate residues, a concentration gradient is formed, directed from the smaller volume (and high local substrate concentration) of the upper compartment toward the larger volume and substrate-free lower compartment.

Discussion

All available evidence suggests that in the absence of BtuF and vitamin B_{12} , BtuCD constantly hydrolyzes ATP^{30,36–38}. In this transport-uncoupled conformational cycle, the NBDs fully open and close and the L172 gate residues fluctuate between their lower-occluding and upper-open positions (Fig. 6e, steps I and II). The cytoplasmic gate opens and closes, yet the movement of the TMDs is mostly restricted to their cytoplasmic side, whereas their periplasmic side maintains its outward-facing conformation. BtuF has the highest affinity to nucleotide-free BtuCD^{26,37,45}, and therefore BtuF likely docks to apo BtuCD. Docking of BtuF initiates the transport-coupled conformational cycle, which begins with the BtuF-driven gradual constriction of the periplasmic side of the TMDs and is closely followed by the ATP-driven gradual closure of the NBDs (Fig. 6e step III, and first ~ 10 cycles of Fig. 6b). The closure of the NBDs drives the upward movement and opening of the periplasmic gate residues (Fig. 6e step IV), increasing the steric clash with the BtuF-bound vitamin B_{12} . BtuF cannot escape the grasp of BtuCD because the TM2–TM3 loops have now swung back to lock on helices 3 and 8. The vitamin B_{12} binding site in BtuF is now greatly disturbed because of the steric clash with the L172 residues. However, the gate is now open, allowing the passage of vitamin B_{12} to the translocation cavity. This sequence of events demonstrates how ATP binding and hydrolysis may be harnessed to solve the conundrum of the release of a ligand that is bound to the SBP with high affinity⁵⁰ by a transporter that has no measurable substrate affinity³⁷.

Once vitamin B_{12} is transferred to BtuCD, the periplasmic gate closes. The BtuF-driven closure of the periplasmic gate (Fig. 6a) starts at about the same time the cytosolic gate and cytosolic side of the TMDs reach their fully open positions (Fig. 6a,b cycle ~ 65 ; Fig. 6e step V). The NBDs continue to close, in parallel to the continuous squeeze originating from the periplasmic side of the TMDs.

The smFRET data suggest that BtuCD displays tight coupling between ligand binding and conformational changes, showing no

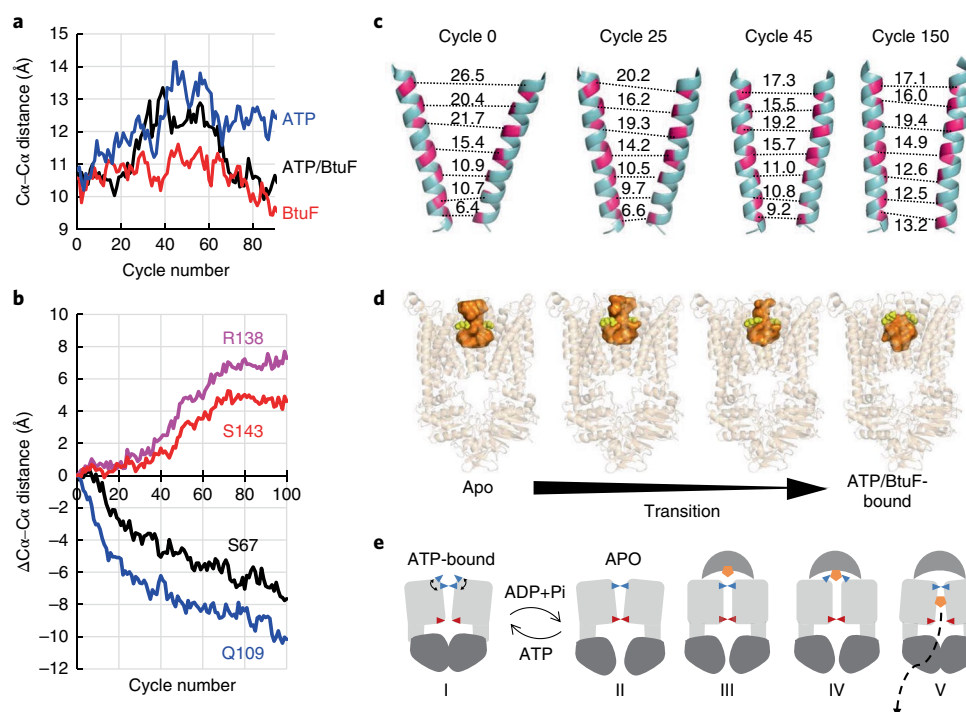


Fig. 6 | Molecular simulations and proposed mechanism of BtuCD. **a**, C α -C α distance between the two periplasmic gate residues (Leu172) during the transition from the apo state to the BtuF-bound (red), ATP-bound (blue), or ATP/BtuF-bound (black) states. Each cycle represents an incremental conformational change along the transition trajectory. **b**, Synchronized closing and opening of the two sides of the TMDs. Shown is the displacement (in Å) of the indicated residues as a function of the step along the transition trajectory (cycle number), during the transition from the apo state to the BtuF/ATP-bound state. S67 is in the NBDs, Q109 is at the periplasmic side of the TMDs, and R138 and S143 are at the cytosolic side of the TMDs. **c**, Movement of the transmembrane helices (5 and 5a) that line the translocation pathway. Shown are snapshots (and distance in Å) of the gradual transition between the apo and the BtuF/ATP-bound states. **d**, Shrinking of the upper compartments of the translocation cavity. BtuCD is shown in a semitransparent cartoon representation, the Met180 residues in yellow spheres, and the cavity in orange volume. Shown are four frames along the gradual conformational transition from the apo to the ATP/BtuF-bound state. **e**, Proposed model for the mechanism of action of BtuCD-F: even in the absence of BtuF and vitamin B₁₂, the NBDs of BtuCD close upon ATP binding, and ATP is hydrolyzed. In this transport-uncoupled conformational cycle (steps I and II), the cytoplasmic side of the TMDs opens and closes, as does the cytosolic gate residues (red triangles). The periplasmic side of the TMDs largely maintain their outward-facing conformation, and the periplasmic gate (blue triangles) fluctuates between their lower-closed and elevated-open states. Docking of BtuF (III) drives the gradual constriction of the periplasmic side of the TMDs, which is shortly followed by the ATP-driven gradual closure of the NBDs. Closure of the NBDs drives the opening and elevation of the periplasmic gate residues (IV), pushing vitamin B₁₂ from BtuF to the translocation cavity. The periplasmic gate re-seals, and at the same time the cytosolic gate and cytosolic side of the TMDs reach their fully open positions (V). In steps III, IV, and V, the constriction at the periplasmic side of the TMDs precedes the relaxation of their cytosolic side, generating a 'squeezing effect' that pushes vitamin B₁₂ toward the intracellular side.

spontaneous conformational changes. It is possible that short-dwell spontaneous fluctuations occur on a time scale that precludes detection. We currently have no data to support or refute this possibility.

In all of the examined conditions, we observed one dominant population of transporter molecules. This conformational uniformity is distinct from the conformational heterogeneity observed for the ABC exporters BmrCD, Pgp, and TM287/288 (refs. 39–41) and from the spontaneous conformational fluctuations of the secondary transporters GltPH and LeuT^{19–22}. Whether this dynamic pattern is unique to BtuCD or shared by other transporters remains to be determined.

The ANM-LD approach allowed us to detect transient conformational changes that are difficult to observe experimentally. We observed that the volume of the upper compartment of the translocation cavity shrinks around vitamin B₁₂, whereas the volume of the lower compartment gradually increases. This creates a *de facto* intramembrane substrate concentration gradient, directed from the periplasm toward the intracellular side. In parallel, a 'squeezing' effect is formed, as the constriction at the periplasmic side precedes the relaxation of the cytoplasmic side. We suggest that these phenomena are important mechanistic aspects that ensure the

directional movement of vitamin B₁₂. Interestingly, the periplasmic gate residue L172 and the Met180 residues that split the translocation cavity into two compartments are highly conserved among BtuCD homologs, as well as in other type-II ABC transporters, suggesting that the proposed mechanism is perhaps generally relevant.

Methods

Methods, including statements of data availability and any associated accession codes and references, are available at <https://doi.org/10.1038/s41589-018-0088-2>.

Received: 23 January 2018; Accepted: 15 May 2018;
Published online: 18 June 2018

References

- Davidson, A. L., Dassa, E., Orelle, C. & Chen, J. Structure, function, and evolution of bacterial ATP-binding cassette systems. *Microbiol. Mol. Biol. Rev.* **72**, 317–364 (2008).
- Slotboom, D. J. Structural and mechanistic insights into prokaryotic energy-coupling factor transporters. *Nat. Rev. Microbiol.* **12**, 79–87 (2014).
- Locher, K. P. Mechanistic diversity in ATP-binding cassette (ABC) transporters. *Nat. Struct. Mol. Biol.* **23**, 487–493 (2016).

4. Møller, S. G., Kunkel, T. & Chua, N.-H. A plastidic ABC protein involved in intercompartmental communication of light signaling. *Genes Dev.* **15**, 90–103 (2001).
5. Rea, P. A. Plant ATP-binding cassette transporters. *Annu. Rev. Plant Biol.* **58**, 347–375 (2007).
6. Oldham, M. L., Davidson, A. L. & Chen, J. Structural insights into ABC transporter mechanism. *Curr. Opin. Struct. Biol.* **18**, 726–733 (2008).
7. Ambudkar, S. V., Kimchi-Sarfaty, C., Sauna, Z. E. & Gottesman, M. M. P-glycoprotein: from genomics to mechanism. *Oncogene* **22**, 7468–7485 (2003).
8. Perez, C. et al. Structure and mechanism of an active lipid-linked oligosaccharide flippase. *Nature* **524**, 433–438 (2015).
9. Parcej, D. & Tampé, R. ABC proteins in antigen translocation and viral inhibition. *Nat. Chem. Biol.* **6**, 572–580 (2010).
10. Vigonsky, E. et al. Metal binding spectrum and model structure of the *Bacillus anthracis* virulence determinant MntA. *Metallomics* **7**, 1407–1419 (2015).
11. Haber, A. et al. L-Glutamine induces expression of *Listeria monocytogenes* virulence genes. *PLoS Pathog.* **13**, e1006161 (2017).
12. Borst, P. & Elferink, R. O. Mammalian ABC transporters in health and disease. *Annu. Rev. Biochem.* **71**, 537–592 (2002).
13. Rees, D. C., Johnson, E. & Lewinson, O. ABC transporters: the power to change. *Nat. Rev. Mol. Cell Biol.* **10**, 218–227 (2009).
14. Scheepers, G. H., Lycklama, A., Nijeholt, J. A. & Poolman, B. An updated structural classification of substrate-binding proteins. *FEBS Lett.* **590**, 4393–4401 (2016).
15. Schneider, E. et al. Receptor-transporter interactions of canonical ATP-binding cassette import systems in prokaryotes. *Eur. J. Cell Biol.* **91**, 311–317 (2012).
16. Khare, D., Oldham, M. L., Orelle, C., Davidson, A. L. & Chen, J. Alternating access in maltose transporter mediated by rigid-body rotations. *Mol. Cell* **33**, 528–536 (2009).
17. Smith, P. C. et al. ATP binding to the motor domain from an ABC transporter drives formation of a nucleotide sandwich dimer. *Mol. Cell* **10**, 139–149 (2002).
18. Eisenmesser, E. Z. et al. Intrinsic dynamics of an enzyme underlies catalysis. *Nature* **438**, 117–121 (2005).
19. Akyuz, N., Altman, R. B., Blanchard, S. C. & Boudker, O. Transport dynamics in a glutamate transporter homologue. *Nature* **502**, 114–118 (2013).
20. Akyuz, N. et al. Transport domain unlocking sets the uptake rate of an aspartate transporter. *Nature* **518**, 68–73 (2015).
21. Zhao, Y. et al. Single-molecule dynamics of gating in a neurotransmitter transporter homologue. *Nature* **465**, 188–193 (2010).
22. Zhao, Y. et al. Substrate-modulated gating dynamics in a Na⁺-coupled neurotransmitter transporter homologue. *Nature* **474**, 109–113 (2011).
23. Gouridis, G. et al. Conformational dynamics in substrate-binding domains influences transport in the ABC importer GlnPQ. *Nat. Struct. Mol. Biol.* **22**, 57–64 (2015).
24. Seo, M.-H., Park, J., Kim, E., Hohng, S. & Kim, H.-S. Protein conformational dynamics dictate the binding affinity for a ligand. *Nat. Commun.* **5**, 3724 (2014).
25. Verhalen, B., Ernst, S., Börsch, M. & Wilkens, S. Dynamic ligand-induced conformational rearrangements in P-glycoprotein as probed by fluorescence resonance energy transfer spectroscopy. *J. Biol. Chem.* **287**, 1112–1127 (2012).
26. Goudsmits, J. M. H., Slotboom, D. J. & van Oijen, A. M. Single-molecule visualization of conformational changes and substrate transport in the vitamin B₁₂ ABC importer BtuCD-F. *Nat. Commun.* **8**, 1652 (2017).
27. Woo, J.-S., Zeltina, A., Goetz, B. A. & Locher, K. P. X-ray structure of the *Yersinia pestis* heme transporter HmuUV. *Nat. Struct. Mol. Biol.* **19**, 1310–1315 (2012).
28. Naoe, Y. et al. Crystal structure of bacterial haem importer complex in the inward-facing conformation. *Nat. Commun.* **7**, 13411 (2016).
29. Locher, K. P., Lee, A. T. & Rees, D. C. The *E. coli* BtuCD structure: a framework for ABC transporter architecture and mechanism. *Science* **10**, 1091–1098 (2002).
30. Borths, E. L., Poolman, B., Hvorup, R. N., Locher, K. P. & Rees, D. C. In vitro functional characterization of BtuCD-F, the *Escherichia coli* ABC transporter for vitamin B₁₂ uptake. *Biochemistry* **44**, 16301–16309 (2005).
31. Klein, J. S. & Lewinson, O. Bacterial ATP-driven transporters of transition metals: physiological roles, mechanisms of action, and roles in bacterial virulence. *Metallomics* **3**, 1098–1108 (2011).
32. Hvorup, R. N. et al. Asymmetry in the structure of the ABC transporter-binding protein complex BtuCD-BtuF. *Science* **317**, 1387–1390 (2007).
33. Korkhov, V. M., Mireku, S. A. & Locher, K. P. Structure of AMP-PNP-bound vitamin B₁₂ transporter BtuCD-F. *Nature* **490**, 367–372 (2012).
34. Korkhov, V. M., Mireku, S. A., Vepriatsev, D. B. & Locher, K. P. Structure of AMP-PNP-bound BtuCD and mechanism of ATP-powered vitamin B₁₂ transport by BtuCD-F. *Nat. Struct. Mol. Biol.* **21**, 1097–1099 (2014).
35. Denisov, I. G., Grinkova, Y. V., Lazarides, A. A. & Sligar, S. G. Directed self-assembly of monodisperse phospholipid bilayer Nanodiscs with controlled size. *J. Am. Chem. Soc.* **126**, 3477–3487 (2004).
36. Livnat-Levanon, N., I Gilson, A., Ben-Tal, N. & Lewinson, O. The uncoupled ATPase activity of the ABC transporter BtuC2D2 leads to a hysteretic conformational change, conformational memory, and improved activity. *Sci. Rep.* **6**, 21696 (2016).
37. Lewinson, O., Lee, A. T., Locher, K. P. & Rees, D. C. A distinct mechanism for the ABC transporter BtuCD-BtuF revealed by the dynamics of complex formation. *Nat. Struct. Mol. Biol.* **17**, 332–338 (2010).
38. Tal, N., Ovcharenko, E. & Lewinson, O. A single intact ATPase site of the ABC transporter BtuCD drives 5% transport activity yet supports full in vivo vitamin B₁₂ utilization. *Proc. Natl. Acad. Sci. USA* **110**, 5434–5439 (2013).
39. Mishra, S. et al. Conformational dynamics of the nucleotide binding domains and the power stroke of a heterodimeric ABC transporter. *eLife* **3**, e02740 (2014).
40. Verhalen, B. et al. Energy transduction and alternating access of the mammalian ABC transporter P-glycoprotein. *Nature* **543**, 738–741 (2017).
41. Timachi, M. H. et al. Exploring conformational equilibria of a heterodimeric ABC transporter. *eLife* **6**, 1–28 (2017).
42. Yaginuma, H. et al. Diversity in ATP concentrations in a single bacterial cell population revealed by quantitative single-cell imaging. *Sci. Rep.* **4**, 6522 (2014).
43. Gregorio, G. G. et al. Single-molecule analysis of ligand efficacy in β₂AR-G-protein activation. *Nature* **547**, 68–73 (2017).
44. Qasem-Abdullah, H., Perach, M., Livnat-Levanon, N. & Lewinson, O. ATP binding and hydrolysis disrupt the high-affinity interaction between the heme ABC transporter HmuUV and its cognate substrate-binding protein. *J. Biol. Chem.* **292**, 14617–14624 (2017).
45. Joseph, B., Jeschke, G., Goetz, B. A., Locher, K. P. & Bordignon, E. Transmembrane gate movements in the type II ATP-binding cassette (ABC) importer BtuCD-F during nucleotide cycle. *J. Biol. Chem.* **286**, 41008–41017 (2011).
46. Joseph, B., Korkhov, V. M., Yulikov, M., Jeschke, G. & Bordignon, E. Conformational cycle of the vitamin B₁₂ ABC importer in liposomes detected by double electron-electron resonance (DEER). *J. Biol. Chem.* **289**, 3176–3185 (2014).
47. Atilgan, A. R. et al. Anisotropy of fluctuation dynamics of proteins with an elastic network model. *Biophys. J.* **80**, 505–515 (2001).
48. Brünger, A., Brooks, C. L. & Karplus, M. Stochastic boundary conditions for molecular dynamics simulations of ST2 water. *Chem. Phys. Lett.* **105**, 495–500 (1984).
49. Ho, B. K. & Gruswitz, F. HOLLOW: generating accurate representations of channel and interior surfaces in molecular structures. *BMC Struct. Biol.* **8**, 49 (2008).
50. Cadieux, N. et al. Identification of the periplasmic cobalamin-binding protein BtuF of *Escherichia coli*. *J. Bacteriol.* **184**, 706–717 (2002).

Acknowledgements

This work is in honor and memory of Yongfang Zhao. The authors thank B. Poolman and A. Meller for fruitful discussions. The plasmid for Cys-less BtuCD was a kind gift from K. Locher (ETH Zurich). This work was supported by grants from NATO Science for Peace and Security Program (SPS Project G4622, O.L., N.L.L., J.R., T.H., B.A., B.A.F., N.B.T., and G.M.), the Israeli Academy of Sciences (O.L., N.L.L.), TUBITAK (The Scientific and Technological Research Council of Turkey) under the grant no 115M418 (T.H., B.A., B.A.F.), the Rappaport Family Institute for biomedical research (O.L., N.L.L., J.R.), the Ministry of Science and Technology (China) “973” Project grant 2014CB910400 (M.Y., J.Z.), the National Natural Science Foundation of China (31522016) (M.Y. and Y.Z.), and the Merieux research foundation (O.L., N.L.L.).

Author contributions

M.Y. performed the smFRET measurements; N.L.L. constructed the mutants and conducted the functional assays; B.A., B.A.F., and J.R. conducted the molecular simulations; G.M. conducted the HOLE analysis; and all authors analyzed data. Y.Z. and O.L. conceptualized the project; Y.Z., O.L., N.B.-T., and T.H. directed the project. O.L. wrote the manuscript with assistance from all authors.

Competing interests

The authors declare no competing interests.

Additional information

Supplementary information is available for this paper at <https://doi.org/10.1038/s41589-018-0088-2>.

Reprints and permissions information is available at www.nature.com/reprints.

Correspondence and requests for materials should be addressed to N.B. or T.H. or O.L.

Publisher's note: Springer Nature remains neutral with regard to jurisdictional claims in published maps and institutional affiliations.

Methods

Statistics. All experiments were repeated in at least three independent experiments, and the reported values are mean \pm s.d. Error bars of histograms represent s.d. obtained by a bootstrap estimation approach with 100 samples. Comparison of two distributions was performed with the Kolmogorov–Smirnov test.

Molecular simulations. To explore the conformational transition pathways connecting functional states of BtuCD, we designed a hybrid molecular simulation methodology, ANM–LD, which integrates a low-resolution α -carbon-based anisotropic network model (ANM)³⁷ with stochastic all-atom implicit solvent Langevin dynamics (LD) simulations⁴⁸. ANM–LD utilizes the structure's intrinsic dynamics to guide functional conformational changes through the cycles of perturbations on the system in its dynamic (ANM) modes toward a target conformation, while taking advantage of the evaluation of the interactions and energetics of the system followed by short time LD simulations. The time window in ANM–LD simulations does not reflect the real time of the simulated transitions, yet provides information on the transition mechanism and the order of events that cannot be achieved with current computational methods such as molecular dynamics (MD) simulations. Moreover, having accessible internal dynamics as the only bias toward the target conformation enables the disclosure of physical and biological transition pathways.

In the present work, starting from the apo state of BtuCD (PDB ID 1L7V)²⁹, three series of ANM–LD runs were performed toward the following target conformations: (i) the ATP-bound structure (PDB ID 4R9U)³⁴, (ii) the ATP/BtuF-bound structure (PDB ID 4F13)³³, and (iii) the BtuF-bound structure (PDB ID 2QI9)³². In the simulations, nucleotides and BtuF were removed from the PDB structures of BtuCD. The r.m.s. deviations of the final conformations from the target crystal structures were 1.4 Å, 1.5 Å, and 1.3 Å for the above mentioned conformational transitions, respectively. We observed very good repeatability in the conformational trajectory of a given transition in parallel simulations and present the results for a representative ANM–LD run.

In the hybrid framework of ANM–LD, an in-house program is used for the ANM calculations and consecutive call-outs of energy minimization and LD simulation steps to be performed in Amber 11-Sander⁵¹ biomolecular simulation package.

ANM–LD simulation protocol. With given initial and target structures, ANM–LD constructs the Hessian matrix for the current initial structure at each iteration cycle by setting a distance threshold radius ($R_{\text{cut}} = 13$ Å) to define the neighbor interactions between α -carbon atoms. The pseudoinverse of the Hessian matrix reveals 3N–6 intrinsic modes of motion⁴⁷. By the application of a deformation factor ($DF = 0.2$ Å), an orthogonal transformation of the system is done in the ANM mode that overlaps most with the difference vector between the structurally aligned initial conformation of the current cycle and the target conformation. The resulting conformation is energy minimized for 500 steps and the generated perturbations on the system are relaxed by following 100 steps LD simulation of 0.2 fs length at temperature $T = 310$ K with the damping constant $\gamma = 5$ ps⁻¹. The time length (20 fs = 100 steps \times 0.2 fs) corresponds to the relaxation time of the perturbed structure by LD in each cycle. ANM and LD steps are iteratively performed until r.m.s. deviation to target conformation reaches a plateau. The schematic outline of ANM–LD method is given in Supplementary Fig. 8.

Validation of ANM–LD. ANM–LD simulations were run for a diverse data set of proteins from nonglobular to globular proteins, including membrane proteins (MalFGK transporter, the sarcoendoplasmic reticulum Ca²⁺-ATPase (SERCA), Usher protein FimD, and ClyA), where conformational transitions from initial RMSDs as high as 14 Å or 24 Å were predicted up to 1.4 Å r.m.s. deviation from their target states, using only the dynamic modes which are accessible to the structure and provided by ANM.

All PDB based figures and trajectory movies for ANM–LD simulation transition were created using PyMOL 1.3 (The PyMOL Molecular Graphics System, Version 1.3, Schrodinger, LLC.). Visualization of the translocation cavity was done using HOLLOW⁴⁹.

Generation of Cys-less BtuCD and insertion of single cysteines. The plasmid encoding a nearly Cys-less BtuCD (which contains only Cys279) was a kind gift from K. Locher (ETH Zurich). We replaced this last endogenous cysteine with a serine residue by site-directed mutagenesis using QuikChange Lightning site-directed mutagenesis kit (Agilent Technologies). We then inserted single cysteine residues into this complete cys-less BtuCD. All mutations/expression vectors were verified by sequencing before analysis.

Expression and purification of recombinant proteins. Single cysteine substitution mutants of BtuCD were expressed and purified as wild-type BtuCD, essentially as performed before^{29,36,37}. Flag-BtuF was purified from osmotic shock extracts by size-exclusion chromatography.

BtuCD labeling. Cy3 and Cy5 maleimide (GE Healthcare) were mixed at a 1:1 molar ratio, and the dye mixture was then added to the single cysteine variants

to obtain a final dye:protein molar ratio of 10:1. Following 1 h incubation at 4 °C, the free dyes were removed by desalting and used immediately for imaging (for experiments and detergent) or reconstituted into nanodiscs and then imaged. To measure the labeling efficiency, a single dye (Cy3 or Cy5) was added at a final dye:protein molar of 10:1. Following 1 h incubation at 4 °C, the free dyes were removed by re-absorption to Ni-NTA beads followed by extensive washing. The labeled proteins were eluted with 250 mM imidazole, which was subsequently removed using a PD-10 desalting column with a MWCO of 7 kDa (Thermo Scientific). The labeling efficiency was then calculated using the known protein concentration, the Cy3 and Cy5 absorbance, and their respective extinction coefficients (Cy3_{550nm}, 150,000 M⁻¹ cm⁻¹; Cy5_{650nm}, 250,000 M⁻¹ cm⁻¹).

Functional assays. In vivo vitamin B₁₂ utilization assays were performed as described in ref. ³⁸. ATP hydrolysis was measured using Molecular Probes EnzCheck kit as described in refs ^{36,38}, and BtuF binding to BtuCD was measured in a Biacore T200 platform (GE healthcare) as elaborated in refs ^{36,37}.

Calorimetric measurements were performed with the MicroCal ITC200 System (GE Healthcare) at 25 °C. Changes in heat were recorded during a series of 20 injections of 2 μ L aliquots of 70 μ M ATP (in the absence of Mg²⁺) into 200 μ L of 6.7 μ M BtuCD in 50 mM Tris–HCl, pH 7.5, 150 mM NaCl, and 0.1% LDAO.

The reconstitution of BtuCD followed our established protocols^{37,38,52}, using a protein:lipid ratio of 1:50 (W/W) and a 3:1 mixture of *E. coli* lipids and egg yolk PC. Detergent was removed by absorption to SM-2 biobeads (Bio-Rad), pre-activated by washing with methanol, ethanol, and double-distilled water.

The proteoliposomes were then mixed with the components of an ATP regenerating system (50 mM Tris–HCl pH 7.5, 150 mM NaCl, 2 mM MgCl₂, 25 mM creatine phosphate, 2.5 mg/mL creatine kinase, and 2 mM ATP), and the mixture was frozen in liquid nitrogen and thawed in a room temperature (20–22 °C; three cycles), followed by 11 extrusions through polycarbonate filters (400 nm). The proteoliposomes were then washed once with ice-cold 50 mM Tris–HCl pH 7.5 and 150 mM NaCl and kept on ice until use. Import of vitamin B₁₂ into liposomes was measured at 33 °C essentially as we have done in the past using the rapid filtration method³⁸, using 10 μ M ⁵⁷Co-vitamin B₁₂ (8 μ Ci/mL; MP Biomedicals), 0.2 μ M BtuCD, and 1 μ M BtuF. The amount of ⁵⁷Co-vitamin B₁₂ retained by the liposomes after a 20-min incubation was determined by gamma radiation counting.

Reconstitution of BtuCD into nanodiscs. The reconstitution of BtuCD into nanodiscs was performed essentially as described^{34,36}. Briefly, BtuCD single-cys variants (prelabeled in detergent solution) were mixed with a membrane scaffold protein (MSP1-E3D1) and a 3:1 mixture of *E. coli* lipids and egg yolk PC to obtain a final molar ratio of 1:8:400 (BtuCD:MSP1-E3D1:lipids). The lipids were presolubilized with 4% Triton X-100 and bath-sonicated until clarity. The final concentration of Triton X-100 was adjusted to 1%, and following 45 min of gentle tilting in 22 °C, pre-activated Biobeads (see above) were added at 250 mg/mL. The beads were replaced twice by fresh ones after 15 min, and again after 30 min.

Anisotropy measurements. The steady state fluorescence anisotropy (r) was measured in bulk (HITACHI F-7000 spectrofluorometer) for Cy3 and Cy5 free in solution or attached to the single-cys variants of BtuCD. For the latter experiments, detergent-solubilized or nanodisc-reconstituted BtuCD was labeled with a single dye. The excitation and emission wavelengths were 554 nm and 568 (Cy3) and 646 nm and 662 (Cy5).

Single-molecule FRET imaging experiments. Single-molecule FRET imaging experiments were carried out as described at refs ^{21,22}. Glass coverslips and imaging chambers were passivated by a mixture of PEG and biotin-PEG and then coated by streptavidin (Invitrogen, 0.1 mg/mL). For imaging in detergent, the surface was further incubated with Biotin-NTA-Ni²⁺, following by incubation with 10–20 nM His-tagged labeled BtuCD. BtuCD nanodiscs were directly immobilized to the streptavidin-coated surface via biotin-PE.

Imaging was performed in 50 mM Tris–HCl, pH 7.5, 150 mM NaCl, 0.1% LDAO, and an oxygen scavenging system consisting of 56 mM glucose, 100 nM glucose oxidase, 1.5 μ M catalase, and 1 mM cyclooctatetraene. Detergent was omitted for imaging of the nanodiscs. To trap the ATP-bound state, either 1 mM adenosine 5'-(β , γ -imido) triphosphate (AMP-PNP, Sigma)/1 mM MgCl₂ or 1 mM ATP/50 μ M EDTA were added. To trap the intermediate state of ATP hydrolysis ATP, vanadate, and MgCl₂ were all added at 1 mM. To determine the effects of binding of BtuF, the BtuCD-F complex was preformed and isolated by size-exclusion chromatography essentially as previously described^{30,37}. Where appropriate, the preformed BtuCD-F complex was reconstituted into nanodiscs. Alternatively, in both detergent solution and in nanodiscs, 1–10 μ M (as indicated) BtuF was added directly to the imaging buffer. Identical results were obtained with both protocols. Fluorescence experiments were performed with a microscope objective-based total internal reflection fluorescent (TIRF) microscope, which is equipped with five lasers (405 nm, 488 nm, 532 nm, 561 nm and 647 nm) and two cooled EMCCD (Andor iXon Ultra). Photons emitted from the Cy3 and Cy5 dyes were collected using 1.49 NA 100 \times objective (Olympus UAPON 100 \times OTIRF), and Optosplit II (Cairn Research Limited) was used to separate spatially Cy3 and Cy5 frequencies. Fluorescence data were acquired by Metamorph software

(Universal Imaging Corporation). Unless otherwise indicated, images were taken at 50 ms/frame.

Single-molecule FRET data analysis. Data analysis was performed essentially as previously described^{21,22}, using the Software SPARTAN⁵³. The Cy3 and Cy5 channels were mapped using TetraSpeck fluorescent microsphere beads (Invitrogen, 0.1 μm). At least 10 beads were selected to get the transformation matrix for mapping by MatLab. Photobleaching events in each trace were detected as a significant drop (≥ 3 times s.d. of background noise) in the median filtered (window size = 9 frames) total fluorescence intensity ($I_{\text{total}} = I_{\text{Cy3}} + I_{\text{Cy5}}$) without returning to the previous average level. Signal-to-noise ratios (SNR) were calculated as total intensity relative to the s.d. of background noise: $I_{\text{total}} / [\text{stdev}(I_{\text{Cy3}}) + \text{stdev}(I_{\text{Cy5}})]$. Traces were selected to meet the following criteria: a single catastrophic photobleaching event, at least 8:1 signal-to-background noise ratio, a donor-to-acceptor Pearson's correlation coefficient < 0 . Spectral bleed-through of Cy3 intensity on the acceptor channel was corrected by subtracting 7.5% of donor signal from the acceptor. FRET traces were calculated as: $\text{FRET} = I_{\text{Cy3}} / (I_{\text{Cy3}} + I_{\text{Cy5}})$, where I_{Cy3} and I_{Cy5} are the instantaneous Cy3 and Cy5 fluorescence intensities, respectively. Contribution of the photophysical zero-FRET state in FRET histograms was removed by fitting the data to a two-state model ($E_1 = 0.1 \pm 0.1$ and $E_2 = 0.4 \pm 0.1$) with the segmental k-means algorithm⁵⁴.

Reporting Summary. Further information on experimental design is available in the Nature Research Reporting Summary linked to this article.

Code availability. In-house MATLAB scripts for the ANM-LD algorithm will be provided upon reasonable request.

Data availability. The data that support the findings of this study are available from the corresponding authors on reasonable request.

References

- Case, D. A. et al. *AMBER 11* (University of California, San Francisco, 2010).
- Vigonsky, E., Ovcharenko, E. & Lewinson, O. Two molybdate/tungstate ABC transporters that interact very differently with their substrate binding proteins. *Proc. Natl Acad. Sci. USA* **110**, 5440–5445 (2013).
- Juette, M. F. et al. Single-molecule imaging of non-equilibrium molecular ensembles on the millisecond timescale. *Nat. Methods* **13**, 341–344 (2016).
- Qin, F., Auerbach, A. & Sachs, F. Estimating single-channel kinetic parameters from idealized patch-clamp data containing missed events. *Biophys. J.* **70**, 264–280 (1996).

Reporting Summary

Nature Research wishes to improve the reproducibility of the work that we publish. This form provides structure for consistency and transparency in reporting. For further information on Nature Research policies, see [Authors & Referees](#) and the [Editorial Policy Checklist](#).

Statistical parameters

When statistical analyses are reported, confirm that the following items are present in the relevant location (e.g. figure legend, table legend, main text, or Methods section).

n/a Confirmed

- The exact sample size (n) for each experimental group/condition, given as a discrete number and unit of measurement
- An indication of whether measurements were taken from distinct samples or whether the same sample was measured repeatedly
- The statistical test(s) used AND whether they are one- or two-sided
Only common tests should be described solely by name; describe more complex techniques in the Methods section.
- A description of all covariates tested
- A description of any assumptions or corrections, such as tests of normality and adjustment for multiple comparisons
- A full description of the statistics including central tendency (e.g. means) or other basic estimates (e.g. regression coefficient) AND variation (e.g. standard deviation) or associated estimates of uncertainty (e.g. confidence intervals)
- For null hypothesis testing, the test statistic (e.g. F , t , r) with confidence intervals, effect sizes, degrees of freedom and P value noted
Give P values as exact values whenever suitable.
- For Bayesian analysis, information on the choice of priors and Markov chain Monte Carlo settings
- For hierarchical and complex designs, identification of the appropriate level for tests and full reporting of outcomes
- Estimates of effect sizes (e.g. Cohen's d , Pearson's r), indicating how they were calculated
- Clearly defined error bars
State explicitly what error bars represent (e.g. SD, SE, CI)

Our web collection on [statistics for biologists](#) may be useful.

Software and code

Policy information about [availability of computer code](#)

Data collection

Fluorescence data were acquired by Metamorph software ver. 7.5 (Universal Imaging Corporation).

Data analysis

smFRET data analysis was performed using the software SPARTAN ver. 3.4 (<https://www.scotttblanchardlab.com/software>)

For manuscripts utilizing custom algorithms or software that are central to the research but not yet described in published literature, software must be made available to editors/reviewers upon request. We strongly encourage code deposition in a community repository (e.g. GitHub). See the Nature Research [guidelines for submitting code & software](#) for further information.

Data

Policy information about [availability of data](#)

All manuscripts must include a [data availability statement](#). This statement should provide the following information, where applicable:

- Accession codes, unique identifiers, or web links for publicly available datasets
- A list of figures that have associated raw data
- A description of any restrictions on data availability

The data that support the findings of this study are available from the corresponding authors upon reasonable request.

Field-specific reporting

Please select the best fit for your research. If you are not sure, read the appropriate sections before making your selection.

Life sciences Behavioural & social sciences

For a reference copy of the document with all sections, see [nature.com/authors/policies/ReportingSummary-flat.pdf](https://www.nature.com/authors/policies/ReportingSummary-flat.pdf)

Life sciences

Study design

All studies must disclose on these points even when the disclosure is negative.

Sample size	<input type="text" value="The sample size of the smFRET experiments is indicated in the figures. All functional assays were performed in triplicates"/>
Data exclusions	<input type="text" value="smFRET traces that did not meet the predefined criteria where excluded, as detailed in the methods section."/>
Replication	<input type="text" value="All experiments were repeated at least three times. The reported values are mean +/- standard deviations."/>
Randomization	<input type="text" value="NA"/>
Blinding	<input type="text" value="NA"/>

Materials & experimental systems

Policy information about [availability of materials](#)

n/a	Involvement in the study
<input checked="" type="checkbox"/>	<input type="checkbox"/> Unique materials
<input checked="" type="checkbox"/>	<input type="checkbox"/> Antibodies
<input checked="" type="checkbox"/>	<input type="checkbox"/> Eukaryotic cell lines
<input checked="" type="checkbox"/>	<input type="checkbox"/> Research animals
<input checked="" type="checkbox"/>	<input type="checkbox"/> Human research participants

Method-specific reporting

n/a	Involvement in the study
<input checked="" type="checkbox"/>	<input type="checkbox"/> ChIP-seq
<input checked="" type="checkbox"/>	<input type="checkbox"/> Flow cytometry
<input checked="" type="checkbox"/>	<input type="checkbox"/> Magnetic resonance imaging